Biomedicine & Pharmacotherapy 192 (2025) 118619

Contents lists available at ScienceDirect

Biomedicine & Pharmacotherapy

journal homepage: www.elsevier.com/locate/biopha

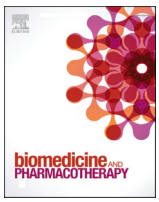

Feasibility and efficacy of electromotive intraperitoneal drug delivery: A hybrid study

Nidda Saeed [a,h,1,2], Hooman Salavati [a,e,1,3], Jolene Wong Si Min [c,4], Sarah Cosyns [a,5], Katrien Remaut [d,6], Charlotte Debbaut [e,7], Mieke Adriaens [f,8], Annelies Coene [g,9], Wim Ceelen [a,b,h,10,*]

[a] Department of Human Structure and Repair, Ghent University, Ghent, Belgium
[b] Department of GI Surgery, Ghent University Hospital, Ghent, Belgium
[c] Department of Sarcoma, Peritoneal & Rare Tumors, National Cancer Centre, Singapore
[d] Lab General Biochemistry and Physical Pharmacy, Ghent University, Ghent, Belgium
[e] IBiTech–BioMMedA, Faculty of Engineering and Architecture, Ghent University, Ghent, Belgium
[f] Department of Chemistry, Ghent University, Ghent, Belgium
[g] Department of Electromechanical, Systems and Metal Engineering, Faculty of Engineering and Architecture, Ghent University, Ghent, Belgium
[h] Cancer Research Institute Ghent (CRIG), Belgium

ARTICLE INFO

Keywords:
Electromotive enhanced drug administration
Iontophoresis
Intraperitoneal
Peritoneal
Drug delivery

ABSTRACT

Intraperitoneal drug delivery (IPDD) is increasingly used to treat peritoneal metastases (PM). However, the adverse biomechanical properties of tumor tissue, such as elevated interstitial fluid pressure and matrix stiffness, are known to impede the transport and efficacy of small-molecule anticancer drugs and nanoparticles (NPs). Physical methods may enhance tissue penetration after IPDD treatment. In this study, we explored the use of an electrical direct current (DC) field generated by electromotive drug administration (EMDA) as a novel physical method to enhance tissue penetration after IPDD. This method involves the combination of a fluid column with a pulsed DC current. A novel in vitro setup was developed in combination with a computational fluid dynamics (CFD) model to test the effects of different treatment variables on the penetration of 100 and 200 nm positively charged NPs in healthy porcine peritoneal samples. We found that tissue penetration using EMDA improved with increasing current intensity, higher temperature of the carrier fluid, and longer administration time, with a plateau reached at 30 min. Isotonic carrier fluids performed better compared to hypotonic and hypertonic solutions. Using these optimized parameters, in vivo studies were performed in both healthy and tumor-induced rats, where peritoneal tissues from all animals and tumor samples from the tumor-induced group were evaluated. EMDA was well tolerated and resulted in significantly enhanced penetration of 100 nm NPs, achieving deeper and more uniform distribution within healthy peritoneum and tumor nodules, irrespective of the anatomical location. These findings highlight EMDA as a promising approach to overcome intrinsic transport barriers of PM and underscore its potential to improve the efficacy of intraperitoneal NP-based therapy for peritoneal metastases.

* Correspondence to: Department of Human Structure and Repair, Ghent University Hospital, Route 1275, Corneel Heymanslaan 10, Ghent B-9000, Belgium
E-mail address: wim.ceelen@ugent.be (W. Ceelen).
[1] Equal contribution.
[2] ORCID: 0000–0001-7576–4150
[3] ORCID: 0000–0001-5398–4646
[4] ORCID: 0000–0002-9750–5755
[5] ORCID: 0000–0002-5173–4296
[6] ORCID: 0000–0002-2244–1339
[7] 0000–0003-1962–238X
[8] ORCID: 0000–0003-4034–1881
[9] ORCID: 0000–0003-4280–8991
[10] ORCID: 0000–0001-7692–4419

https://doi.org/10.1016/j.biopha.2025.118619
Received 21 August 2025; Received in revised form 11 September 2025; Accepted 1 October 2025
Available online 3 October 2025

1. Introduction

Patients with intra-abdominal cancer are at risk of developing peritoneal metastasis (PM), which is characterized by a specific pathophysiology and is known to be relatively therapy-resistant [1]. Intraperitoneal (IP) administration of cytotoxic drugs is widely used in the treatment of peritoneal metastases [2]. However, a major drawback of intraperitoneal delivery is the limited penetration of the instilled drug into the tumor tissue; typically, only the outer cell layers are effectively exposed [3–6]. Therefore, pharmacological and physical interventions, including the use of hyperthermia, elevated intraperitoneal pressure, and stromal targeting drugs, have been tested to enhance the tissue penetration of IP drugs [7,8]. In parallel, nanosized active compounds have been used for IP delivery to enhance peritoneal retention and drug exposure time [9].

An interesting potential method to enhance drug penetration after IP delivery is to use an electrical force to drive the drug into the tumor tissue along an electrical potential gradient. The use of electrical forces in conjunction with drug delivery is known as electromotive drug administration (EMDA) and is based on three main electrokinetic phenomena: electromigration, electroosmosis, and electroporation [10]. The combined effect of electromigratory and electroosmotic forces is termed iontophoresis, which describes enhanced drug transport through the application of an electric current in an electrolyte drug solution [11]. In electromigration, drug ions are repelled by an oppositely charged electrode, and the resulting ionic flux across the tissue to maintain electric neutrality enhances drug transport [12]. Non ionized drugs are dependent on electroosmosis, referring to enhanced drug transport resulting from the electric current induced convective flow of water [13]. Finally, electroporation describes the formation of aqueous pores by the application of an electric current, which increases the permeability of membranes and facilitates drug delivery [14].

The main clinical use of EMDA is the treatment of ophthalmological and skin diseases [15,16]. Recently, EMDA was combined with intravesical chemotherapy to treat non-muscle invasive bladder cancer [17]. In vitro and in vivo studies have shown that EMDA enhances the penetration of Mitomycin C into all layers of the bladder wall [18,19]. The clinical efficacy of EMDA to enhance drug delivery has been demonstrated in three randomized controlled trials in bladder cancer [20–22].

We hypothesized that EMDA could enhance intraperitoneal nanoparticle transport beyond the limitations of passive diffusion. To test this hypothesis, we established a multi-tiered framework comprising computational modeling, in vitro validation, and in vivo application. Computational and in vitro models were developed in parallel, allowing reciprocal refinement of the electrokinetic parameters. The model simulated nanoparticle transport via electromigration and electroosmosis, and the in vitro system enabled real-time quantification across tissue-mimetic barriers. For in vivo studies, two nanoparticle platforms were employed to reflect distinct translational goals: amine-modified fluorescent nanoparticles, commonly used in bioimaging and mechanistic transport studies due to their charge-tunable surfaces and optical traceability [23] were used to assess regional biodistribution in healthy peritoneum, while siRNA-RNAiMAX lipoplexes, representing clinically relevant therapeutic nanocarriers for gene silencing [24], were applied in a syngeneic colorectal PM model to evaluate tumor-specific delivery. This dual-system design allowed us to explore both the fundamental transport dynamics and therapeutic relevance of EMDA, supporting its application across multiple nanoparticle classes.

2. Materials & methods

2.1. In vitro model development

The in vitro apparatus consisted of a plastic liquid-containing cylinder (outer diameter, 90 mm; inner diameter, 84 mm; height, 240 mm) combined with a metallic base plate and an electrode connected to a current generator (*Physionizer® Mini 30N2, Medolla, Italy)*. The filling height of the cylinder was measured using a ruler. Four 1 cm^2 round openings were milled into the base plate to accommodate the tissue samples (Fig. 1). Removable plastic rings were used to secure the tissue samples. The current intensity ranged from 0 to 30 mA constant or pulsed direct current (DC, 2.0 kHz) with a maximum rise rate of 100 μA/s with an initial value of 0 mA until a maximum current of 30 mA was reached.

A removable top cover enabled the introduction of a temperature probe and a modified 16 F silicon bladder catheter containing a custom-made platinum spiral electrode. The device was equipped with a detachable outer water jacket, allowing the instilled liquid to be heated.

2.2. Computational model development

A computational fluid dynamics (CFD) model was developed to predict solute penetration into the tissue (Fig. 2), replicating the conditions of the in vitro experiments. The model geometry, parameter values, boundary conditions, and initial conditions were chosen based on the properties of the in vitro model and the physical laws governing ionic transport. The spatiotemporal change in tissue concentration can be described as

$$\frac{dc_i}{dt} = D\nabla^2 c_i + z_i u_i FE\nabla c_i - u\nabla c_i \tag{1}$$

Where c_i [a.u.] and D [m^2/s] are the ion's concentration and diffusion coefficient, respectively. z_i, F and E [V/m] represent the ion's charge number, Faraday's constant, and the electric field. u [m/s] is the interstitial fluid velocity described by Darcy's law, and the ion mobility u_i [mol.s/kg] is described by Einstein's relation:

$$u = -\frac{k}{\mu}\nabla P \tag{2}$$

$$u_i = \frac{D}{k_B T} \tag{3}$$

Where k [m^2], μ [Pa.s], *and* P [Pa] represent the tissue permeability, buffer dynamic viscosity, and hydrostatic pressure, respectively. k_B [J/mol.K] and T [K] are Boltzmann constant and absolute temperature, respectively. Ion diffusion D is described by the Stokes-Einstein equation:

$$D = \frac{k_B T}{6\pi\mu r_h} \tag{4}$$

where r_h [m] is the hydrodynamic radius of the nanoparticles. The dependency of μ on the carrier solution temperature (T_c [°C]) and salinity (S [kg/kg]) can be described by the following empirical relationship [25]:

$$\mu = \mu_w\left(1 + AS + BS^2\right) \tag{5}$$

Where

$$\mu_w = 4.3 \times 10^{-5} + \frac{1}{0.16(T_c + 65) - 91.3} \tag{6}$$

$$A = 1.5 + 2 \times 10^{-2} T_c - 9.5 \times 10^{-5} {T_c}^2 \tag{7}$$

$$B = 8 - 7.6 \times 10^{-2} T_c + 4.7 \times 10^{-4} {T_c}^2 \tag{8}$$

The electrical current in the system was modeled using the law of conservation of charge:

$$\nabla . J = Q \tag{9}$$

Where:

$$J = \sigma E + \epsilon_r \frac{\partial E}{\partial t} \quad (10)$$

where Q is the current source, J is the current density, σ is the electrical conductivity [S/m], and ϵ_r is the relative permittivity. The electric field, E, is defined as:

$$E = -\nabla V \quad (11)$$

Where V [V] is the electric potential. The numerical values of all the parameters used in the simulation are listed in Table 1.

Given the symmetrical configuration of the in vitro apparatus, a 2D model was developed with a top width of 300 μm and thickness of 500 μm. The electrode was positioned at the top of the tissue, maintaining a defined distance of 1 cm (baseline) between the electrode and the tissue. A hydrostatic pressure head of 5 mmHg (baseline value) was incorporated by simulating the water column above the tissue. The concentration source (i.e., 1 a.u.) was also applied to the top boundary of the tissue. No-flow and no-flux conditions were assigned to the side and bottom boundaries, respectively. For the electric field, insulation boundary conditions were applied to the sides, while the bottom boundary was set to ground. The models were developed using COMSOL Multiphysics (COMSOL, Inc., Burlington, USA) based on the described computational domain and parameters (Fig. 2).

2.3. Tissue samples and nanoparticles

Fresh, unprocessed porcine peritoneal specimens were harvested from the interior aspect of the ventral abdominal wall and cut into 1.0 cm circular specimens using a stainless steel punch (SMI AG, St Vith, Belgium). Positively charged amine-modified polystyrene fluorescent nanoparticles (NPs) with diameters of 100 nm ($\lambda_{excitation}$ = 475 nm; $\lambda_{emission}$ = 540 nm, Sigma Aldrich, Saint Louis, USA) and 200 nm ($\lambda_{excitation}$ = 580 nm; $\lambda_{emission}$ = 605 nm, *FluoSpheres*^{TM}, Thermo Fisher Scientific, Carlsbad, USA) were used. The nanoparticles were sonicated (2510 Branson Sonicator, Marshall Scientific, Hampton, New Hampshire, USA) and diluted to a concentration of 1:1000. Positively charged fluorescent NPs were selected because of the negatively charged nature of the peritoneum, which enhances their attraction and interaction under the influence of an applied electric field.

2.4. Experimental procedures and comparisons

The effect of the following variables on NP tissue penetration was studied using both the in vitro experimental model and computational model: EMDA current intensity (passive diffusion, 10, 20, and 30 mA), EMDA duration (10, 20, 30, 40, and 60 min), carrier solution (0.9 % NaCl, 0.45 % NaCl, 3 % NaCl, and peritoneal dialysate (Physioneal 40® Glucose 1.36 %, Baxter, Ontario, Canada)), temperature (20, 37, and 42°C), hydrostatic pressure (5 and 10 mmHg), NPs diameter (100 and 200 nm), and distance from the tip of the electrode to the tissue surface (1, 2, and 3 cm). Parameter values were selected based on clinical relevance, prior optimization studies (including conductivity and cytocompatibility assessments), and alignment with established EMDA protocols used in bladder cancer therapy. Experiments were performed sequentially and in triplicate, and within each experiment, only a single parameter was varied, while the other experimental conditions remained constant.

2.5. Assessment of nanoparticle tissue penetration

After each experiment, peritoneal tissue samples were embedded in optimal cutting temperature (OCT) compound embedding medium (Leica Microsystems, Machelen, Belgium), placed in pre-cooled isopentane, and cryosectioned to a thickness of 20 μm. Cryosections were equilibrated at room temperature, fixed in acetone, washed with Dulbecco's phosphate-buffered saline (DPBS-, Fisher Scientific, Merelbeke, Belgium), and secured with Vectashield mounting medium (Vector Laboratories, Inc., Burlingame, California, USA). Cryosections were imaged using a fluorescence confocal microscope (Nikon A1R, Nikon Instruments Inc., Amstelveen, The Netherlands) at 20X magnification, and the images were processed and analyzed using ImageJ (version 1.51, National Institutes of Health, Bethesda, Maryland, USA).

For depth-resolved analysis, rectangular regions of interest (ROIs) of 300 × 100 μm^2 were systematically placed at predefined depths from

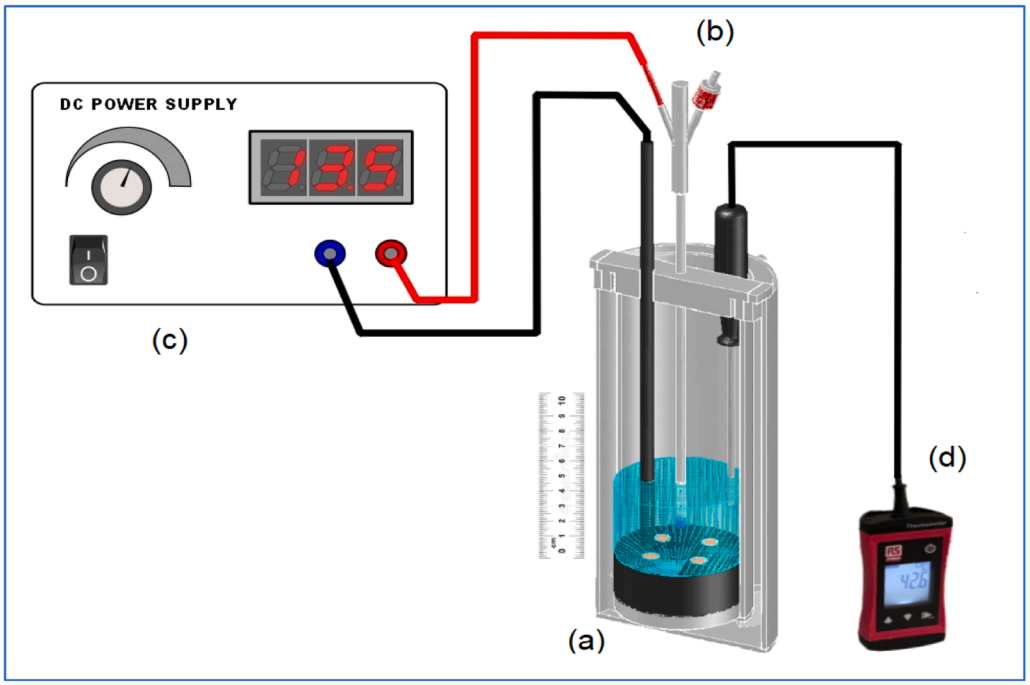

Fig. 1. In vitro EMDA setup: (a) partially insulated conductive apparatus comprising a silver base plate, (b) spiral platinum electrode, (c) DC current generator, and (d) temperature probe.

the exposed peritoneal surface: 0–100 μm (ROI 1), 101–200 μm (ROI 2), and 201–300 μm (ROI 3). ROI placement was aligned perpendicularly to the tissue surface, and in cases of curved or irregular geometry, digital adjustment was applied in ImageJ to maintain perpendicularity. To minimize sampling bias, triplicate sets of ROIs were drawn at fixed 500 μm intervals across each cryosection, providing standardized spatial coverage. Prior to fluorescence measurement, brightness and contrast were normalized across all images to reduce background variability. Fluorescence was expressed as mean fluorescence intensity (MFI) per ROI (Fig. 3).

As a measure of the total tissue NP, we calculated the proportion of stained (%) fluorescent NPs in the histological slices. A single ROI was drawn around the border of the specimen, and the number of pixels in this ROI was calculated. Thereafter, a color threshold was set to select yellow-green colored pixels, and the proportion (%) of fluorescent pixels over total pixels was calculated as follows:

$$proportion\ stained(\%) = \frac{number\ of\ fluorescent\ pixels\ in\ ROI}{total\ number\ of\ pixels\ in\ ROI} \times 100\%$$

2.6. Animal model of EMDA

2.6.1. Animals

Male Wistar Albino Glaxo (WAG)-Rij rats (10–12 weeks old, weight $\geq$ 200 g) were purchased from Envigo (Horst, The Netherlands). Animals were allowed to acclimatize to the surroundings for at least 7 days and were kept in standard housing conditions with water and food ad libitum in a temperature- and humidity-controlled room with 12-hour light/dark cycles. The animal experiments were approved by the Animal Ethics Committee of the Faculty of Medicine of Ghent University (ECD 22–41) and were performed according to relevant Belgian and European animal welfare regulations.

2.6.2. In vivo EMDA model

The experiments were performed under general anesthesia with sevoflurane (Sevorane™, Abbott, Waver, Belgium; 8 % at induction and 4 % maintenance). Analgesia was administered subcutaneously with ketoprofen (5 mg/kg). The abdominal and dorsal areas were shaved and disinfected with 70 % ethanol. The animals were positioned supine, and their limbs were fixed using adhesive tape. Pads moistened with NaCl 0.9 % were placed on the dorsal skin with a layer of Media gel (Farla Medical, Antwerp, Belgium) between the pads and skin to ensure adequate electrical conductivity. A 5 mm midline incision was made just below the rib arch, and a 5 mm balloon trocar was inserted (Applied Medical, Amersfoort, The Netherlands). The modified bladder catheter containing the platinum electrode was advanced through the trocar into the peritoneal cavity (Fig. 4). Using a bladder catheter, the peritoneal cavity was slowly filled with 50 mL of carrier solution. Filling the peritoneal cavity resulted in moderate abdominal distention. The current and voltage were alternately monitored throughout the procedure using a digital multimeter. Vital parameters (blood oxygen saturation, heart rate, and respiratory rate) were continuously monitored using a MouseOx® Plus device (Starr Life Sciences, Oakmont, PA, USA).

Table 1
Parameter values used in the numerical simulation.

Parameter	Description		Value/ Range	Reference
z_i	Charge number		1	-
$F\ [C/mol]$	Faraday's constant		96,485	-
$k\ [m^2]$	Tissue permeability		2.8E−16	[26]
$P\ [mmHg]$	Hydrostatic pressure		5 – 10	-
$k_B\ [J/K]$	Boltzmann constant		1.38E−23	-
$r_h\ [nm]$	Nanoparticles radius		50 – 100	-
$\sigma\ \left[\frac{S}{m}\right]$	Electrical conductivity	Tissue	0.4	[27]
		Saline	1.52 – 8.83	[28]
ϵ_r	Relative permittivity	Tissue	81.8	[29]
		Saline	70.2 – 79.9	[30]

First, a feasibility study was performed in four animals to evaluate the technical safety and tolerability of the EMDA. The procedure was performed using positive or negative polarity pulsed direct current and isotonic (NaCl 0.9 %) or hypotonic (NaCl 0.45 %) saline carrier solutions for 20 min. Inverted polarity was tested because of its potential relevance when using compounds with a negative charge; however, in the current study, only positively charged NPs were used. The current amplitude was gradually increased starting from 1 mA to determine the maximally tolerable current. Postoperative pain and discomfort were assessed using the Rat Grimace Scale (RGS), based on specific facial action units [29]. Animal weights were recorded until one week after the procedure.

Based on the findings of the feasibility study, the EMDA experiment was set up as follows: animals (N = 3 per group) received IP instillation of 100 nm NPs in NaCl 0.9 % and were allocated at random to passive diffusion alone or to EMDA using the optimal settings identified in the feasibility study. The EMDA sequence was initiated with a current output accuracy of ± 0.2 mA.

At the end of the EMDA procedure, the remaining NP solution was aspirated using a syringe, and the catheter and trocar were removed. Parietal peritoneal biopsies were performed at four anatomical locations: the right upper abdomen (RUA), left upper abdomen (LUA), right fossa (RF), and left fossa (LF). Humane euthanasia was performed using T-61 (0.3 mL/kg, intravenously).

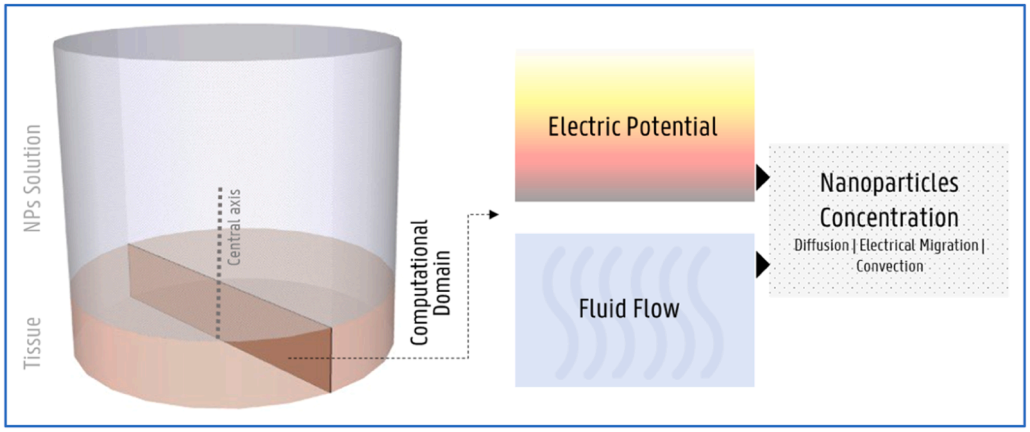

Fig. 2. CFD EMDA setup illustrating the computational domain. Fluid flow and electrical potential modules are linked to the nanoparticle transport module, incorporating diffusion, electrical migration, and convection.

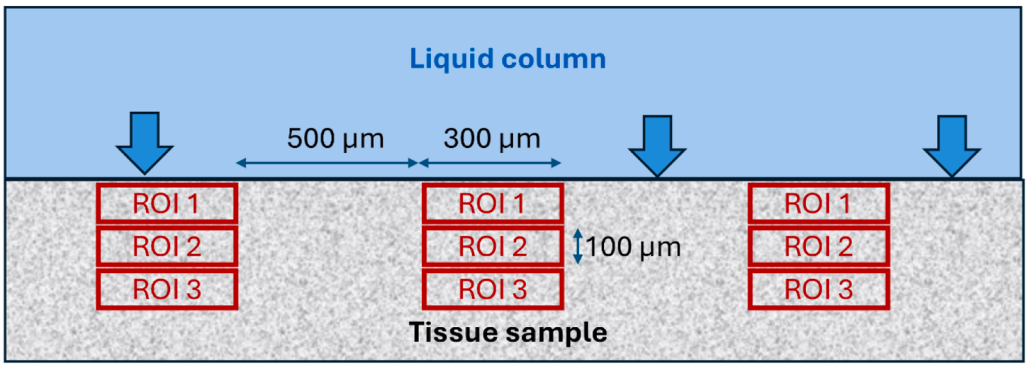

Fig. 3. Measurement of tissue penetration of fluorescent nanoparticles. ROI, region of interest.

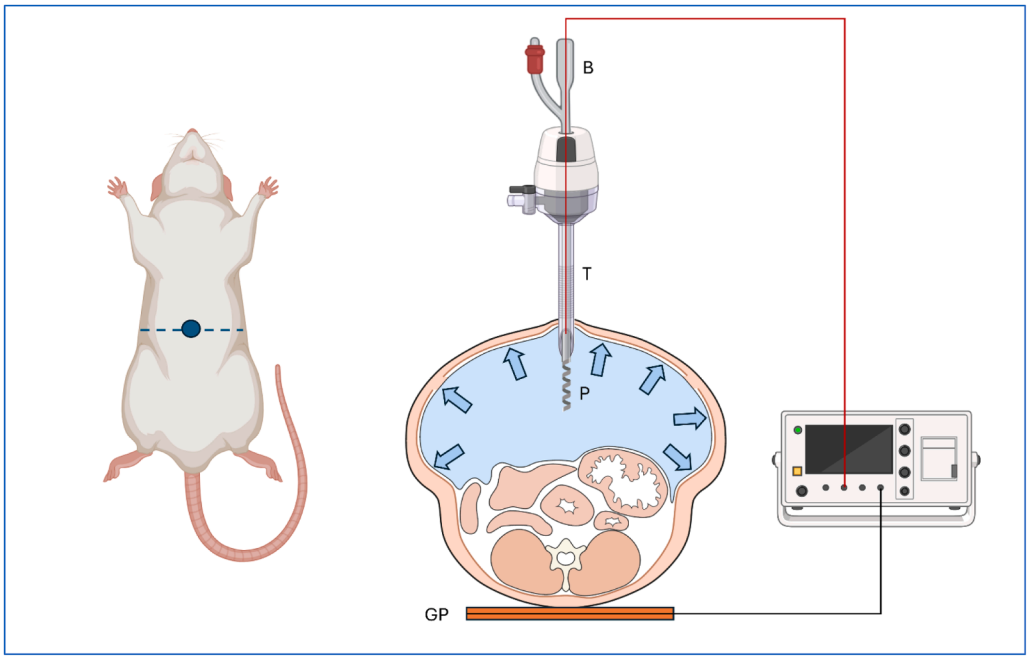

Fig. 4. Rat model of intraperitoneal electromotive drug administration (EMDA). B, bladder catheter; T, 5 mm trocar; P, spiral platinum electrode; GP, grounding plate.

2.6.3. In vivo colorectal PM EMDA model

To investigate the effect of EMDA on nanoparticle penetration, peritoneal metastases were established using syngeneic CC531s.2 colon adenocarcinoma cells, which were generously provided by the Laboratory of Experimental Oncology (University of Antwerp, Belgium). Cells were cultured in RPMI 1640 medium (Thermo Fisher Scientific) supplemented with 10 % fetal bovine serum (Sigma-Aldrich, Netherlands) and maintained at 37 °C in a humidified atmosphere containing 5 % CO_2. Prior to inoculation, the cells were verified to be free of mycoplasma and rat-specific viral contaminants. Animals were intraperitoneally injected with 2×10^6 CC531s.2 cells suspended in 1 mL of RPMI medium, targeting the left lower abdominal quadrant, as previously described [31]. Body weight and clinical conditions were monitored daily to assess animal welfare.

2.6.4. Preparation of nanoparticle formulations

Cy5-labeled luciferase siRNA (Cy5-siRNA; Eurogentec, Searing, Belgium) and Lipofectamine RNAiMAX (Invitrogen, USA) were separately diluted in OPTI-MEM® medium (Sigma-Aldrich Louis, USA). siRNA-lipoplexes were formed by mixing equal volumes of the diluted siRNA (final concentration 0.19 µM) and diluted RNAiMAX (N/P ratio of 3), followed by incubation at room temperature for 5 min. The resulting complexes were subsequently diluted in OPTI-MEM® to a final siRNA concentration of 33 nM and further diluted in sterile saline to a final volume of 50 mL.

2.6.5. Physicochemical characterization of nanoparticles

The hydrodynamic diameter and zeta potential of siRNA-RNAiMAX lipoplexes were measured using a Zetasizer® Nano ZS (Malvern Instruments, Malvern, UK) after appropriate dilution. Particle size distribution was determined by dynamic light scattering (DLS) at 25 °C in Milli-Q® water with a backscattering detection angle of 173°. Zeta potential of siRNA-RNAiMAX complexes was assessed via electrophoretic light scattering (ELS) under the same conditions.

2.6.6. EMDA procedure and tumor tissue sampling

In tumor-bearing animals, EMDA was applied using the same procedural parameters as those previously established for non-tumor-bearing controls. Following treatment, both peritoneal tumor tissue and adjacent parietal peritoneum biopsies were collected to assess NPs distribution under EMDA-enhanced conditions. Tumor nodules were classified into two size-based categories: macroscopic lesions (>1 cm in diameter) and micronodular lesions (<1 cm), to enable the evaluation of size-dependent penetration. Anatomical localization was stratified into

four predefined intraperitoneal regions: right upper abdomen (RUA), left upper abdomen (LUA), right iliac fossa (RF), and left iliac fossa (LF).

This dual-level sampling framework, based on both tumor size and anatomical site, was designed to support quantitative comparisons of nanoparticle accumulation across heterogeneous tumor microenvironments. Harvested tissues were cryosectioned and processed according to established protocols. Fluorescence imaging was performed under standardized acquisition parameters, and quantitative image analysis was conducted using validated algorithms to determine the regional and nodular nanoparticle distribution profiles.

2.7. Statistical analysis

Quantitative results are presented as means (standard deviations). Data distribution was assessed for normality using QQ plots and formally tested using the Shapiro - Wilk procedure. Groups were compared using two-way repeated-measures analysis of variance (ANOVA), followed by Tukey's correction for multiple comparisons. The Pearson correlation coefficient was calculated to assess the correlations between the experimental parameters. All p-values were 2-sided. Statistical analyses and plotting were performed using GraphPad Prism 8.30 (GraphPad Software, La Jolla, USA).

3. Results

3.1. In vitro effect of electrical current

Experiments were performed at the following fixed settings: duration of 20 min, carrier solution NaCl 0.9 %, hydrostatic pressure of 5 mmHg, and temperature of 20°C using 200 nm positively charged fluorescent nanoparticles (NPs).

Compared with passive diffusion, EMDA significantly increased the tissue penetration of fluorescent NPs, and a higher current magnitude resulted in increased penetration, specifically when a current of 30 mA was applied (Fig. 5A). In addition, total NP uptake was strongly correlated with current magnitude (r = 0.8, Fig. 5B). The computational results confirmed a positive correlation between current magnitude and NP penetration, with the most pronounced effect observed at ROI 2 (Fig. 5C and D).

3.2. In vitro effect of EMDA duration

Experiments were performed at a constant current of 30 mA, using NaCl 0.9 %, a hydrostatic pressure of 5 mmHg, and a temperature of 20°C using 200 nm positively charged fluorescent NPs.

A time-dependent increase of NP penetration was observed until a duration of 30 min, however, further extension of EMDA duration did not affect peritoneal tissue penetration (p = 0.0003, Fig. 6A). A weak correlation was found between EMDA duration and total NP uptake

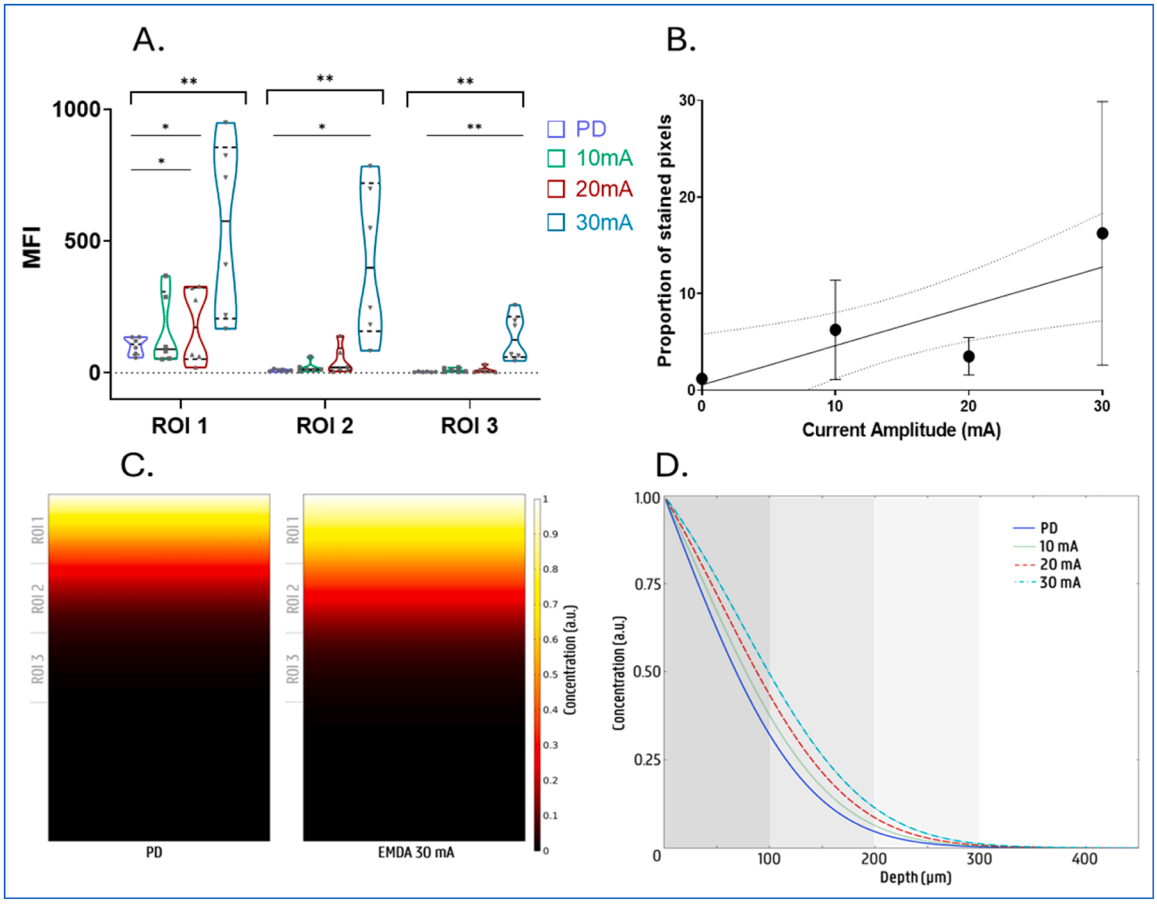

Fig. 5. A: Violin plots of tissue penetration in porcine peritoneum of 200 nm positively charged fluorescent nanoparticles (NP) at varying depths from the exposed surface: 0–100 μm (ROI 1), 101–200 μm (ROI 2), and 201–300 μm (ROI 3) after passive diffusion (PD) and electromotive drug administration (EMDA) at a current of 10, 20, and 30 mA (**, and * indicate $p < 0.01$, and $p < 0.05$, respectively). B: Total NP uptake as measured by the proportion of fluorescent to total number of pixels at the tissue surface during PD and EMDA at a current of 10, 20, and 30 mA respectively. A strong positive correlation was found between the proportion of fluorescent pixels and current magnitude (r = 0.8, p = 0.1) C and D: Results from the computational fluid dynamics (CFD) model. The ROIs 1, 2, and 3 are highlighted with dark, medium, and light grey shades, respectively. MFI, mean fluorescence intensity.

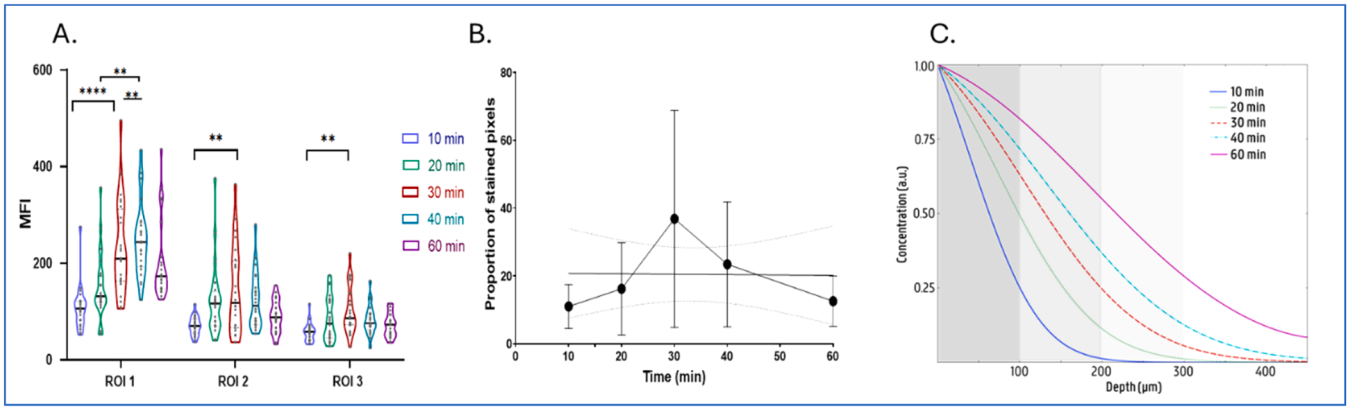

Fig. 6. *A*: Violin plots of tissue penetration in porcine peritoneum of fluorescent nanoparticles (NP) at varying depths: 0–100 μm (ROI 1), 101–200 μm (ROI 2), and 201–300 μm (ROI 3) after electromotive drug administration (EMDA) during 10, 20, 30, 40, and 60 min (****, ***, **, and * indicate $p < 0.0001$, $p < 0.001$, $p < 0.01$, and $p < 0.05$, respectively). B: Total NP uptake at the tissue surface during EMDA over a range of 10–60 min. Maximal NP penetration and uptake were observed in the 30 min group. C: Computational results of the effect of exposure time on NP tissue concentration. The ROIs 1, 2, and 3 are highlighted with dark, medium, and light grey shades, respectively. MFI, mean fluorescence intensity.

($r = 0.5$, $p = 0.3$, Fig. 6B). In contrast, the computational results indicated that NP penetration continued to increase with EMD duration beyond 30 min (Fig. 6C).

3.3. *In vitro effect of carrier solution*

Experiments were performed at a constant current of 30 mA for 20 min, at a hydrostatic pressure of 5 mmHg, and at a temperature of 20°C using 200 nm positively charged fluorescent NPs. NPs penetration did not significantly differ between NaCl 0.9 %, NaCl 0.45 %, and peritoneal dialysis solution. However, NPs penetration was significantly poorer with the use of NaCl 3 %. Total NPs uptake was not significantly different between carrier solutions (Fig. 7 A and B). Similarly, minimal differences were observed in the effect of the carrier solution on penetration depth from the CFD results. Furthermore, consistent with in vitro findings, NaCl 3 % was found to adversely affect NPs tissue concentration compared to the other carrier solutions (Fig. 7C).

3.4. *In vitro effect of carrier solution temperature*

Experiments were performed at a constant current of 30 mA for 20 min, hydrostatic pressure of 5 mmHg, carrier solution NaCl 0.9 %, and using 200 nm positively charged fluorescent NPs. We observed a clear temperature dependence of NP penetration, in all three regions of interest (Fig. 8A). Moreover, higher temperature increased total NP uptake, with the highest uptake observed at 42° (Fig. 8B). The computational model confirmed increasing tissue NP concentration with increasing temperature, with a more pronounced effect in the deeper regions of interest compared to ROI1 (Fig. 8C).

3.5. *In vitro effect of hydrostatic pressure*

Experiments were performed at a constant current of 30 mA for 20 min, at a temperature of 20°C, carrier solution NaCl 0.9 %, using 200 nm positively charged fluorescent NPs. The pressure was varied by changing the height of the liquid column. We found that increasing the hydrostatic pressure did not enhance NP tissue penetration or total NP uptake (Fig. 9A and B). Similarly, the computational model showed no effect of hydrostatic pressure on tissue NP concentration (Fig. 9C).

3.6. *In vitro effect of nanoparticle size*

Experiments were performed at a constant current of 30 mA for 20 min at a temperature of 20°C, carrier solution NaCl 0.9 %, hydrostatic pressure of 5 mmHg and using both 100 and 200 nm positively charged NPs.

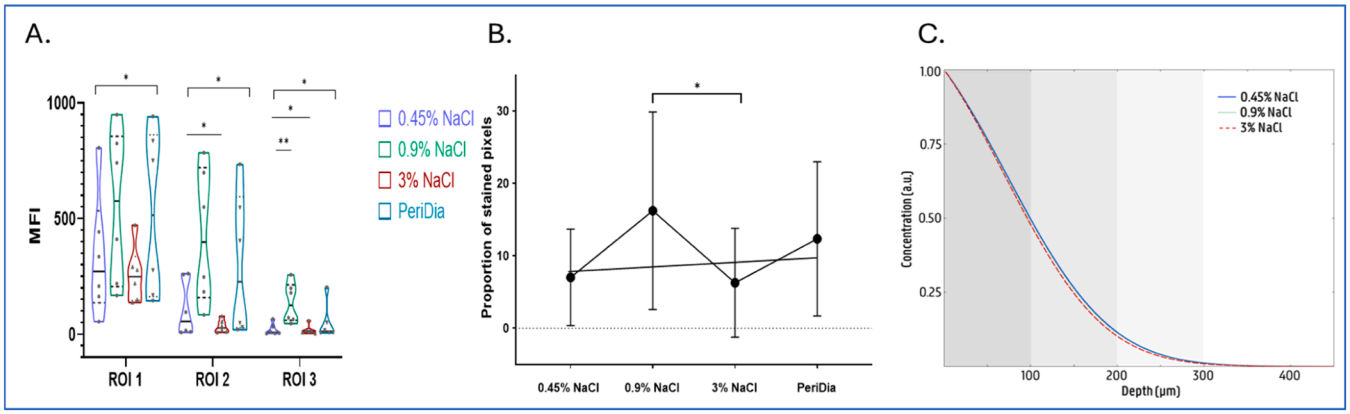

Fig. 7. A: Violin plots of tissue penetration in porcine peritoneum of fluorescent nanoparticles(NPs) at varying depths: 0–100 μm (ROI 1), 101–200 μm (ROI 2), and 201–300 μm (ROI 3) after electromotive drug administration (EMDA) with hypotonic saline (NaCl 0.45 %), isotonic saline (NaCl 0.9 %), hypertonic saline (NaCl 3 %), and peritoneal dialysate solution (PeriDia) (**, and * indicate $p < 0.01$, and $p < 0.05$, respectively). B: Total NP uptake as measured by the proportion of fluorescent to total number of pixels at the tissue surface after EMDA using different carrier solutions. C: The computational results of the effect of carrier solution on NP concentration. The ROIs 1, 2, and 3 are highlighted with dark, medium, and light grey shades, respectively. MFI, mean fluorescence intensity.

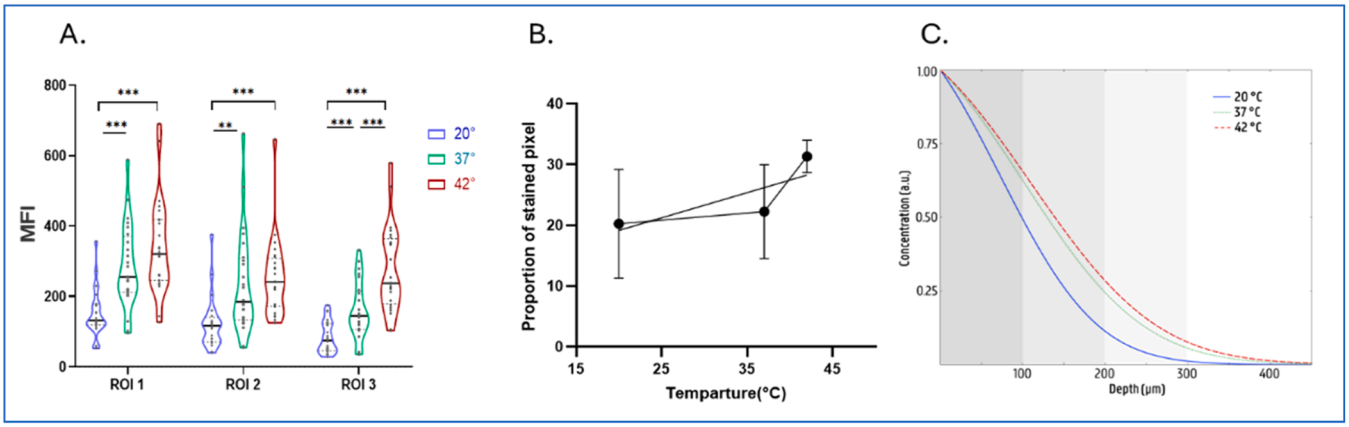

Fig. 8. A: Violin plots of tissue penetration in porcine peritoneum of fluorescent nanoparticles at varying depths: 0–100 μm (ROI 1), 101–200 μm (ROI 2), and 201–300 μm (ROI 3) after passive diffusion and electromotive drug administration at 20°, 37° and 42° (***, **, and * indicate $p < 0.001$, $p < 0.01$, and $p < 0.05$, respectively). B: Total NP uptake as measured by the proportion of fluorescent to total number of pixels at the tissue surface after EMDA at 20°, 37°, and 42° respectively. C: The computational results on the effect of temperature on tissue NP concentration. The ROIs 1, 2, and 3 are highlighted with dark, medium, and light grey shades, respectively. MFI, mean fluorescence intensity.

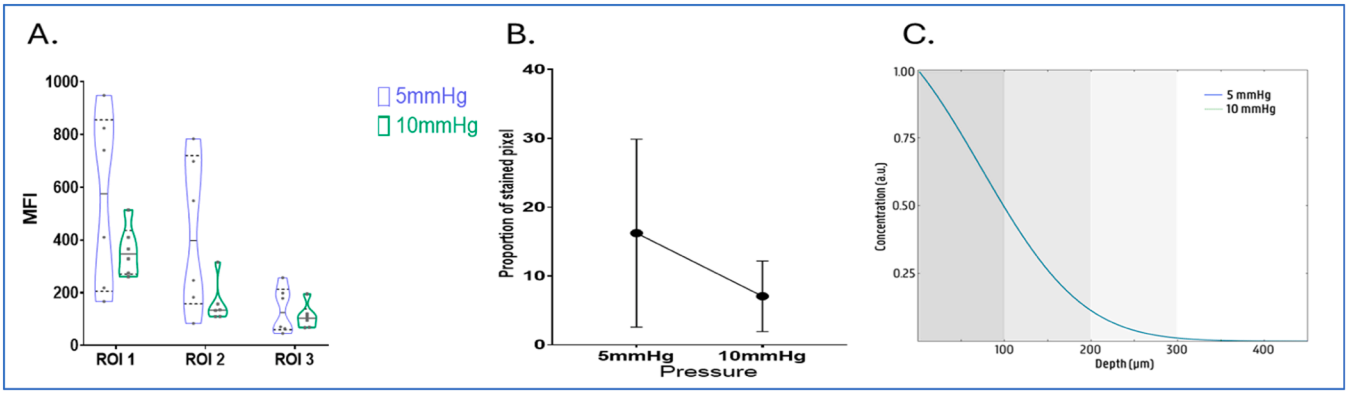

Fig. 9. A: Peritoneal penetration of fluorescent nanoparticles and B: total NP uptake at different hydrostatic pressures. C: The computational results of the effect of hydrostatic pressure on tissue NP concentration. The ROIs 1, 2, and 3 are highlighted with dark, medium, and light grey shades, respectively. MFI, mean fluorescence intensity.

We observed that the 200 nm NPs exhibited a higher penetration in the most superficial ROI, whereas 100 nm NPs were more prevalent in the deeper tissue regions (ROI2 and ROI3) following EMDA (Fig. 10 A and B). The computational model also demonstrated that the smaller NP size resulted in deeper tissue penetration. Notably, when EMDA was applied at 30 mA using 200 nm particles, the resulting penetration was lower than that observed with passive diffusion of 100 nm particles in the CFD model.

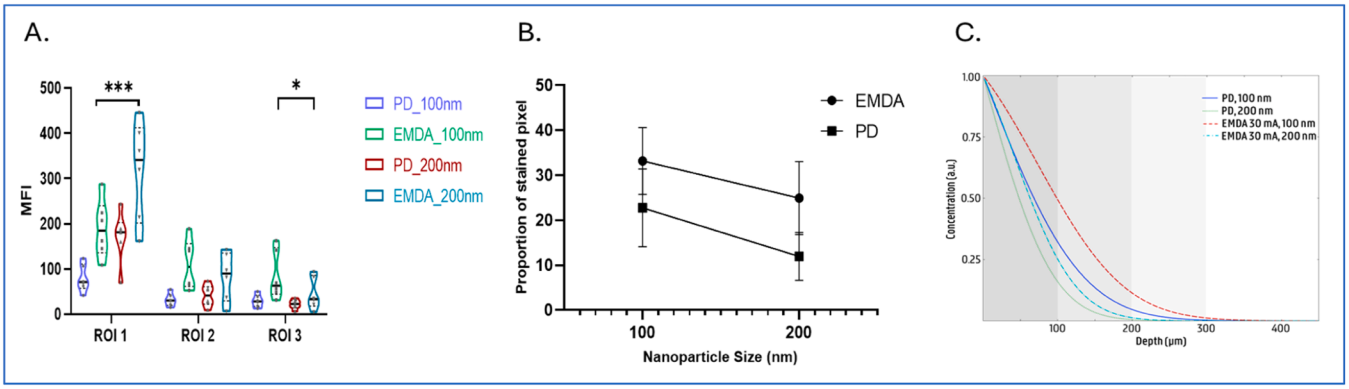

Fig. 10. A: Violin plots of tissue penetration in porcine peritoneum of fluorescent nanoparticles (NPs) (100 and 200 nm) at varying depths: 0–100 μm (ROI 1), 101–200 μm (ROI 2), and 201–300 μm after PD and EMDA (***, **, and * indicate, $p < 0.001$, $p < 0.01$, and $p < 0.05$, respectively). B: Total NPs uptake is measured by the proportion of fluorescent to total number of pixels at various tissue depths using fluorescent NPs of comparable sizes (100 and 200 nm) under passive diffusion (PD) and electromotive drug administration (EMDA). C: The computational results on the effect of nanoparticle size on buffer concentration. The ROIs 1, 2, and 3 are highlighted with dark, medium, and light grey shades, respectively. MFI, mean fluorescence intensity.

3.7. In vitro effect of distance between the electrode tip and tissue distance

Experiments were performed at a constant current of 30 mA for 20 min at a temperature of 20°C, carrier solution NaCl 0.9 %, hydrostatic pressure of 5 mmHg, and using 100 nm positively charged fluorescent NPs. Despite the important dependence of electrical field strength on the distance between electrodes, no significant differences were observed in NP penetration according to the distance between the tip of the electrode and the tissue surface (Fig. 11). The observed difference in ROI2 is likely due to an outlier effect. The computational model confirmed the absence of an effect of electrode-to-tissue distance.

3.7.1. In vivo feasibility of EMDA

EMDA performed at 1.6 mA for 20 mins was well tolerated in all experiments, with no detectable changes in heart rate, respiratory rate, or oxygen saturation. This safety profile was consistent across electrode polarities and independent of the carrier solution used (NaCl 0.9 % or NaCl 0.45 %). When the applied current was increased beyond 1.8 mA, however, muscle twitching was consistently observed, indicating stimulation of the abdominal musculature at higher intensities (Fig. 12).

Postoperatively, the animals gained weight and displayed no signs or symptoms of pain or distress (Table 2).

3.7.2. In vivo efficacy of EMDA

Based on the findings from in vitro experiments and the in vivo feasibility study, EMDA was performed in vivo at a current amplitude of 1.6 mA, with a rise rate of 30 μA/sec for 30 min at body temperature using 100 nm fluorescent NPs. Tissue penetration of fluorescent NPs was assessed with confocal fluorescence microscopy (Fig. 13). Compared to passive diffusion, EMDA resulted in a significantly deeper tissue penetration in all three regions of interest, across samples taken from all four anatomical locations (Fig. 14).

3.7.3. Effect of electrophoresis on the physicochemical characteristics of nanoparticles

The effect of EMDA on the physicochemical characteristics of siRNA-RNAiMAX nanoparticles was assessed using dynamic light scattering and electrophoretic mobility analysis. As shown in Fig. 15, size, zeta potential, and polydispersity index (PDI) were measured before (Pre-EMDA) and after electric field exposure. Prior to EMDA, siRNA-RNAiMAX complexes displayed monodisperse, cationic properties, with an average hydrodynamic diameter of 112 ± 5 nm, a zeta potential of + 16.4 ± 1.3 mV, and PDI of 0.226. Following EMDA, nanoparticle size significantly increased to 191 ± 50 nm ($p < 0.05$), likely due to electric field-induced aggregation or reorganization of the lipoplex structure. This observation was accompanied by a modest rise in PDI to 0.273, which remained within the commonly accepted threshold for monodisperse formulations (PDI < 0.3). Interestingly, while a downward shift in surface charge was observed, from + 16.4 mV to + 8.6 mV, this reduction in zeta potential did not reach statistical significance, suggesting that although surface ion rearrangement occurred, electrostatic stabilization was largely retained. These results indicate that EMDA introduces measurable but controlled alterations in nanoparticle size and surface charge, without compromising colloidal stability. Overall, the findings suggest that siRNA-RNAiMAX NPs remain physically robust and electrically responsive under EMDA conditions, supporting their continued development for electro-enhanced IP delivery.

3.7.4. EMDA efficacy in colorectal PM in vivo model

In tumor-bearing animals, the EMDA protocol was applied identically to that used in healthy rats. Harvested tumor samples harvested were stratified into two groups based on macroscopic size: tumors < 1 cm and tumors > 1 cm, reflecting the heterogeneous tumor burden typically observed, which often includes multiple small nodules alongside one or two larger, vascularized masses. Confocal fluorescence imaging demonstrated that EMDA markedly enhanced NPs delivery into tumor tissues compared to passive diffusion. Quantitative analysis showed a significant increase in mean fluorescence intensity (MFI) across all three depth-defined ROIs in EMDA-treated samples for both tumor size categories (Figs. 17–19).

In smaller lesions (<1 cm), EMDA resulted in deeper and more uniform NP penetration, possibly attributed to reduced interstitial resistance and improved electrical field distribution. Although larger nodules (>1 cm) demonstrated relatively lower MFI values, EMDA still achieved significantly higher tissue penetration compared to passive diffusion ($p < 0.001$). These findings highlight the capacity of EMDA to overcome stromal and architectural barriers in peritoneal metastases, thereby facilitating effective intratumoral delivery of nanoscale therapeutics in both early and advanced stage diseases.

4. Discussion

Peritoneal metastases present a significant therapeutic challenge in cancer medicine, owing to their relative resistance to systemic (intravenous) chemotherapy and their potential to cause debilitating symptoms, including bowel obstruction and ascites. Intraperitoneal drug

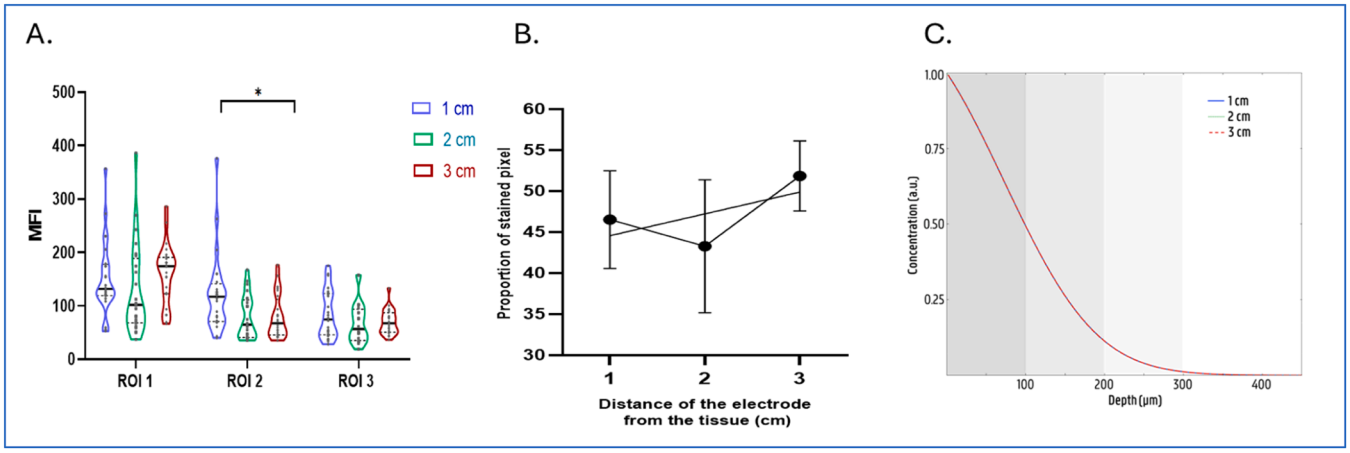

Fig. 11. A: Violin plots of the depth of 100 nm fluorescent nanoparticle (NP) penetration at different distances (1, 2, and 3 cm) between the tip of the platinum electrode and the peritoneal tissue surface after electromotive drug administration (EMDA) (* indicate $p < 0.05$). B: Total NP uptake as measured by the proportion of fluorescent to total number of pixels at the tissue surface after EMDA at different electrode distances (1, 2, and 3 cm) from the peritoneal tissue surface respectively. C: Computational results of the effect of electrode distance on NP penetration. The ROIs 1, 2, and 3 are highlighted with dark, medium, and light grey shades, respectively. MFI, mean fluorescence intensity.

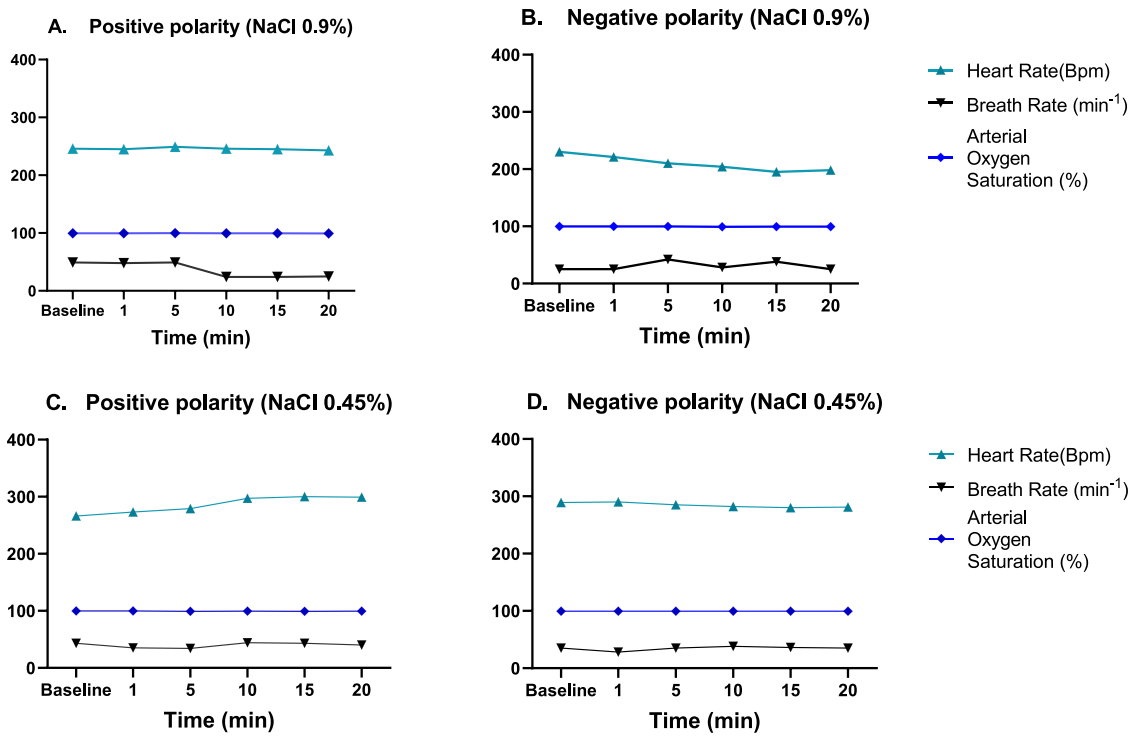

Fig. 12. Heart rate, respiratory rate, and oxygen saturation in rats undergoing 20 min. of electromotive drug administration (EMDA) during 20 min at a current intensity of 1.6 mA using positive or negative polarity and using NaCl 0.9 % or 0.45 % as carrier solution.

Table 2
Effect of electromotive drug administration (EMDA) on postoperative weight, complications, and facial action units from the Rat grimace Scale (RGS, units range from 0 to 2). RGS was assessed in the immediate postoperative period.

Polarity		Carrier Solution	Weight before EMDA (g)	Weight at 1 week post EMDA (g)	Surgical Complications	Orbital Tightening	Nose/Cheek Flattening	Ear Changes (Position, Shape)	Whisker change
+	Rat 1	NaCl 0.9 %	346	362	No	0	1	0	1
	Rat 2		341	364	No	0	1	0	1
-	Rat 1	NaCl 0.45 %	449	466	No	0	0	1	1
	Rat 2		446	461	No	1	0	0	1

delivery has gained an important role in the therapy of PM, particularly in patients with ovarian cancer. However, the efficacy of IP drug delivery is limited by rapid drug clearance from the peritoneal cavity, and by limited tumor tissue penetration due to adverse biomechanical properties including increased stiffness and elevated interstitial fluid pressure [32].

The use of NPs for IP drug delivery is appealing, since they may prolong IP residence time and enable the use multifunctional, targeted compounds [9]. Limited tissue penetration remains a drawback of the use of IP NPs delivery, and several strategies have been experimentally tested to enhance tissue transport. These include targeting the extracellular matrix, modulating cancer cell density with paclitaxel, and employing tumor penetrating peptides [33–35]. In addition, physical methods including internal radiotherapy and hyperthermia have also been shown to enhance NP penetration following IP delivery [36,37].

Here, we explored the use of an electrical force as a physical method to enhance NP penetration after intraperitoneal delivery. Electromotive drug administration (EMDA) is based on electromigration and electroosmosis, and is clinically used in combination with intravesical instillation for early stage bladder cancer and in transdermal drug delivery [17,38]. In order to gain insight into the physical mechanisms that underlie EMDA for intraperitoneal drug delivery, we developed a computational fluid dynamics model in parallel with a novel in vitro setup. In addition, we delivered a proof of concept of the potential of EMDA enhanced IP delivery of NPs in vivo.

We found a dose-dependent impact of current intensity on NP penetration and uptake. Higher current intensities, particularly at 30 mA, significantly increased penetration depth and total uptake compared to lower intensities (10 and 20 mA). These findings are consistent with the principles of electromigration, wherein higher current levels generate stronger ionic fluxes, facilitating enhanced transport of charged particles through tissues [39,40]. Similar findings have been reported with intravesical administration of mitomycin C for bladder cancer, where increased current intensities improved drug penetration into the bladder wall [13,16,41]. However, exceeding safe current thresholds may result in local tissue damage due to pH shifts, thermal effects, or tissue dehydration [17,18]. Thus, while 30 mA emerged as an optimal current intensity in vitro, its feasibility in human patients requires further investigation.

The effect of EMDA increased with exposure time; however, no

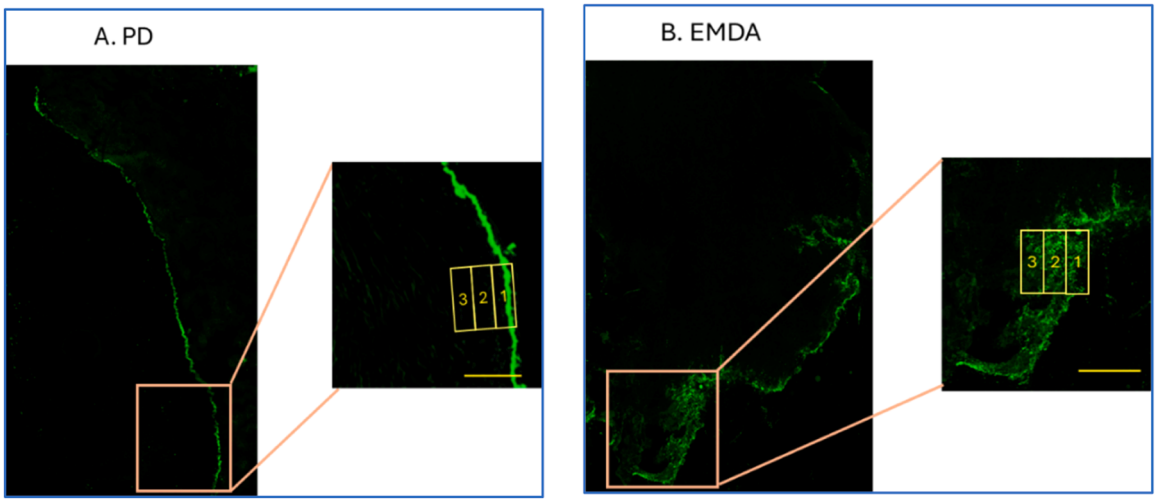

Fig. 13. Representative confocal microscopy images of rat peritoneal tissue after intraperitoneal delivery of 100 nm fluorescent nanoparticles using either (A) passive diffusion (PD) or (B) electromotive drug administration (EMDA). The scale bar represents 500 μm.

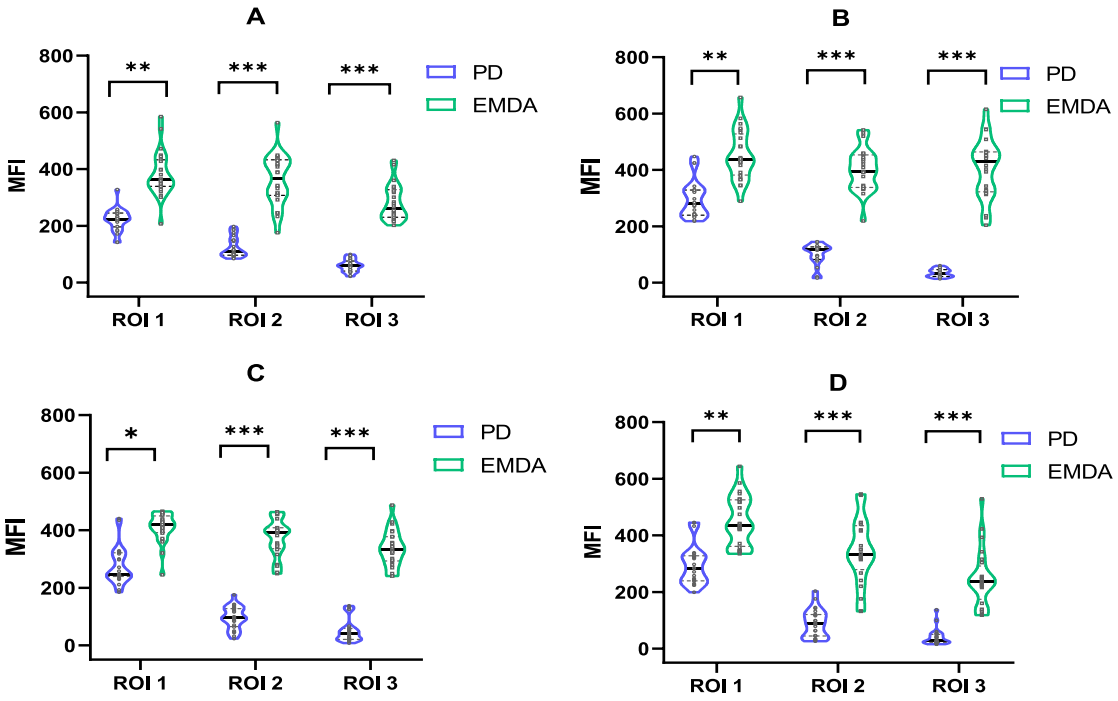

Fig. 14. Violin plots of tissue penetration in rat peritoneum of 100 nm fluorescent nanoparticles at varying depths: 0–100 μm (ROI 1), 101–200 μm (ROI 2), and 201–300 μm (ROI 3) after passive diffusion (PD) and electromotive drug administration (EMDA). Samples were taken after 30 min from four quadrants of the rat peritoneal cavity. A: left upper abdomen (LUA), B: right upper abdomen (RUA), C: left Iliac fossa (LF), and D: right Iliac fossa (RF). (***, **, and * indicate $p < 0.001$, $p < 0.01$, and $p < 0.05$, respectively). MFI, mean fluorescence intensity.

additional enhancement was observed beyond 30 min. This plateau is likely attributed to saturation and an increase in tissue resistance over time. These results are consistent with previous transdermal iontophoresis studies, where prolonged exposure reduced efficacy once steady-state transport was achieved [20,40]. In contrast, the CFD model predicted continued NP penetration with extended exposure. This results from the Nernst-Planck equation, which describes ion transport as the combined effect of concentration gradients and electric fields, where the current-driven transport component is proportional to the product of current and time [19]. The observed discrepancy is likely attributed to fluorescent particle decay in the experimental setup. The results suggest that the required duration of intraperitoneal EMDA application is realistically feasible in clinical application. Current clinical protocols for IP chemotherapy typically involve administration in a 2-liter volume, which is left to resorb spontaneously, a process primarily governed by IP pressure [42].

The choice of carrier solution significantly influenced the efficiency of EMDA. Isotonic saline (0.9 %) and peritoneal dialysate exhibited superior performance compared to hypo- and hypertonic solutions, likely because they maintain electrical neutrality and minimize osmotic disturbances. These findings are consistent with prior studies indicating that isotonic environments enhance electromigration and

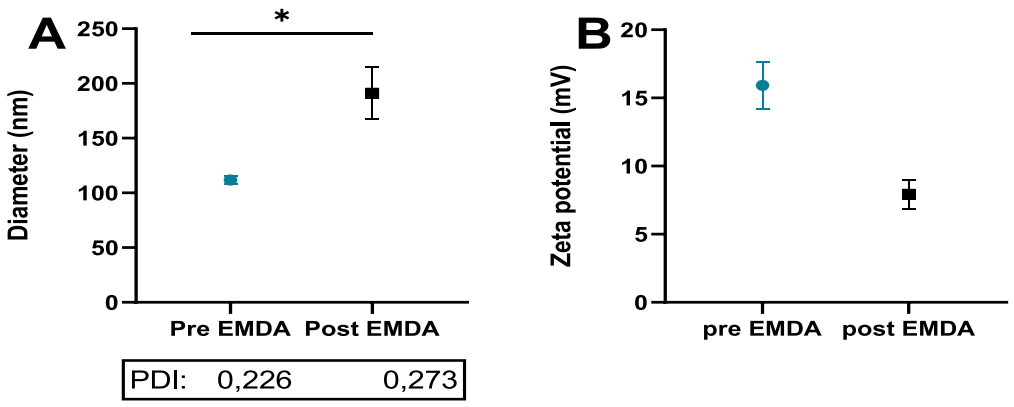

Fig. 15. Graphical representation of siRNA-RNAiMAX nanoparticles (A) size and (B) zeta potential pre and post EMDA procedure in invivo rat model.

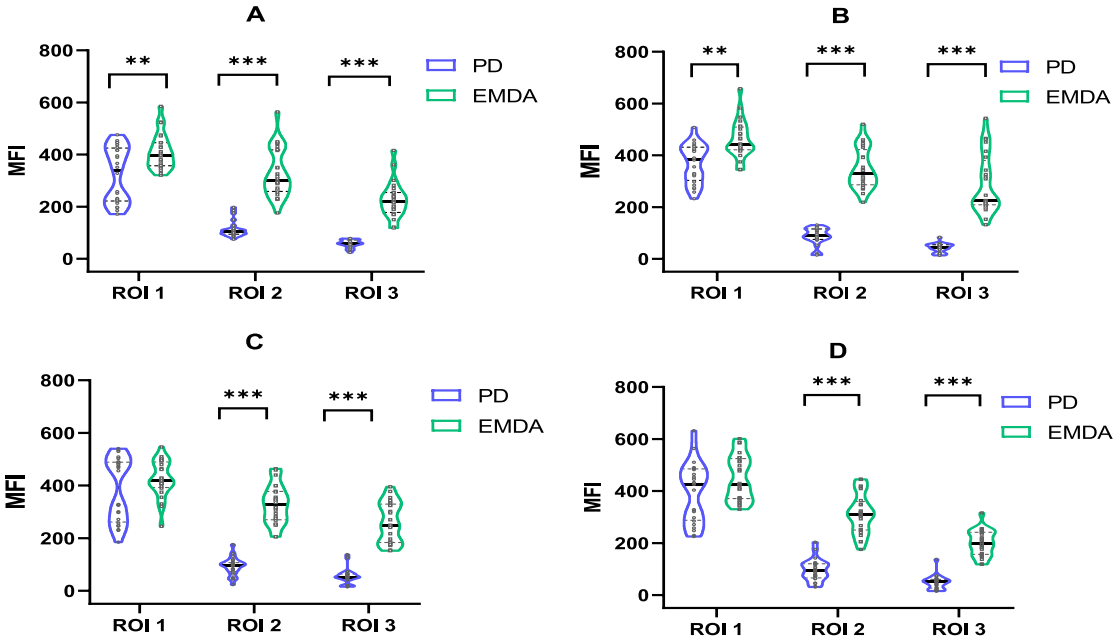

Fig. 16. Violin plots of tissue penetration in rat peritoneum of Cy5-siRNA-RNAiMAX NPs at varying depths: 0–100 μm (ROI 1), 101–200 μm (ROI 2), and 201–300 μm (ROI 3) after passive diffusion (PD) and electromotive drug administration (EMDA). Samples were taken after 30 min from four quadrants of the rat peritoneal cavity. A: left upper abdomen (LUA), B: right upper abdomen (RUA), C: left Iliac fossa (LF), and D: right Iliac fossa (RF). (***, **, and * indicate $p < 0.001$, $p < 0.01$, and $p < 0.05$, respectively). MFI, mean fluorescence intensity.

electroosmotic flow by sustaining ionic fluxes across tissues [40,43]. In contrast, the CFD simulation showed only minimal influence of the carrier solution. A major reason for this might be the influence of salinity on the porosity of the tissue [44,45], which, in turn, affects the effective diffusion of nanoparticles [43]. Mathematical description of this effect is challenging, as no clear consensus exists in the literature, and the influence varies depending on both tissue type and salinity. Hypotonic solutions may compromise tissue integrity, whereas hypertonic solutions may interfere with electroosmotic flow due to osmotic gradients [21]. Thus, careful selection of carrier solutions is critical to optimizing EMDA efficacy, as noted in iontophoresis studies for ophthalmic and dermatological applications [11,12].

Notably, EMDA efficacy was found to be strongly temperature-dependent. Hyperthermia increases tissue permeability by reducing interstitial fluid pressure (IFP) and loosening extracellular matrix components, thereby synergizing with electromigration and electroosmosis to enhance drug transport [22,46]. This synergistic effect has been well-documented in hyperthermic intraperitoneal chemotherapy (HIPEC), where elevated temperatures improve tumor tissue penetration of cisplatin and other chemotherapeutic agents [4,47]. Combining hyperthermia with EMDA thus represents a promising strategy to optimize localized drug delivery, particularly in dense tumor environments such as PM.

Smaller nanoparticles (50–100 nm) showed significantly higher penetration depths and uptake compared to larger particles (>200 nm). This is consistent with the enhanced permeability and retention (EPR) effect, which favors smaller particles for extravasation into interstitial spaces [43]. Additionally, positively charged NPs achieved greater penetration and uptake due to electrostatic attraction with the negatively charged cell membrane, thereby facilitating enhanced tissue interaction [39,48]. Similar trends have been reported in studies of nanoparticle-based drug delivery systems, where smaller particle sizes

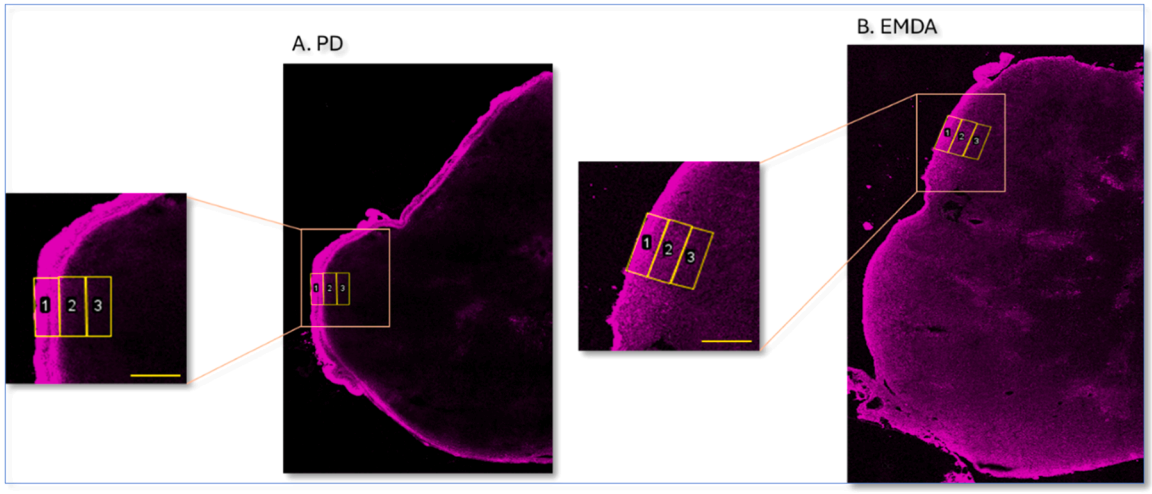

Fig. 17. Representative confocal microscopy images of rat Tumor > 1 cm after intraperitoneal delivery of Cy5-siRNA-RNAiMAX NPs using either (A) passive diffusion (PD) or (B) electromotive drug administration (EMDA). The scale bar represents 500 μm.

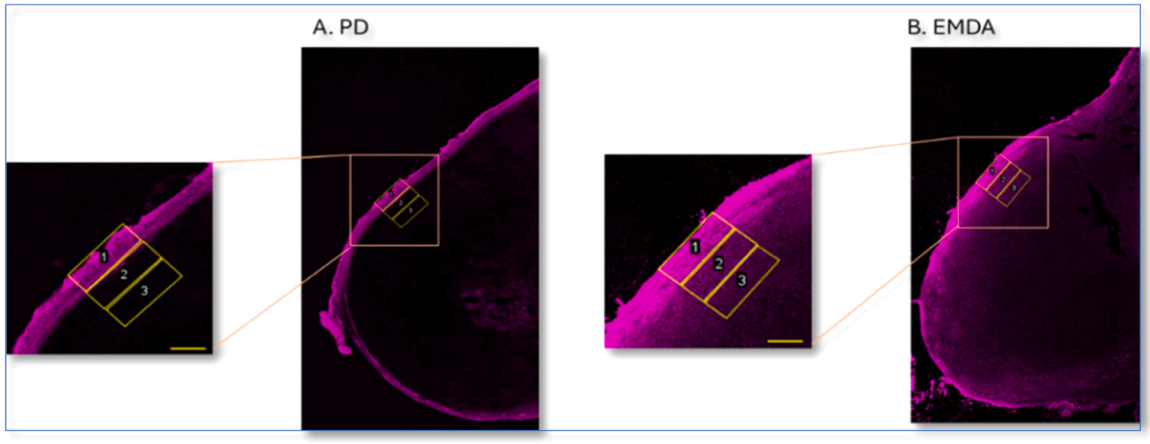

Fig. 18. Representative confocal microscopy images of rat Tumor < 1 cm after intraperitoneal delivery of Cy5-siRNA-RNAiMAX NPs using either (A) passive diffusion (PD) or (B) electromotive drug administration (EMDA). The scale bar represents 100 μm.

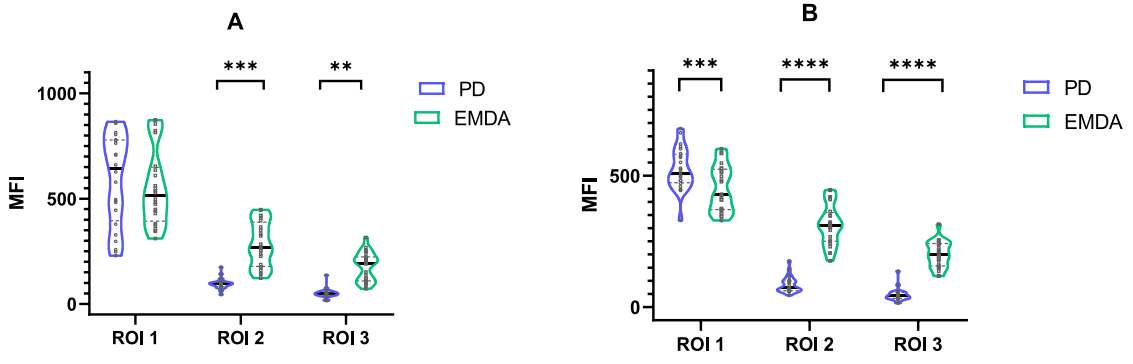

Fig. 19. Violin plots of tissue penetration in rat peritoneum of Cy5-siRNA-RNAiMAX NPs at varying depths: 0–100 μm (ROI 1), 101–200 μm (ROI 2), and 201–300 μm (ROI 3) after passive diffusion (PD) and electromotive drug administration (EMDA). Samples were taken after 30 min from rat peritoneal cavity. A: Tumor > 1 cm, B: Tumor < 1 cm. (***, **, and * indicate $p < 0.001$, $p < 0.01$, and $p < 0.05$, respectively). MFI, mean fluorescence intensity.

and optimized surface charges significantly improved biodistribution and therapeutic efficacy [22,25]. The efficacy of EMDA is influenced by the electric charge of the administered drug. Cationic agents migrate toward the cathode and anionic agents toward the anode under direct current, making the ionization state at physiological pH a key consideration. For example, mitomycin C and doxorubicin, both carrying positive charges under physiological conditions, are well-suited for anodal EMDA. Cisplatin, though neutral in its base form, forms

positively charged species in solution and similarly benefits from anodal application. In contrast, 5-fluorouracil is anionic and may require cathodal delivery for optimal transport. These principles are supported by both experimental and computational studies and highlight the importance of aligning drug properties with the EMDA configuration to improve delivery outcomes [40].

In vivo, EMDA was well tolerated in rats at a current intensity of 1.6 mA. We observed that, compared to passive diffusion, EMDA significantly enhanced NPs penetration and retention in healthy peritoneal tissue samples obtained from four different anatomical locations. By comparison, EMDA used in combination with intravesical delivery typically uses 20 mA. However, the electrical field strength, which is inversely related to square of the distance from the source, is relatively higher in the rat model.

Our observations regarding EMDA-induced changes in siRNA-RNAiMAX nanoparticle properties align with findings of Braet et al [49], who investigated the impact of electrostatic high-pressure nebulization (ePIPAC) on ionic self-assembled nanomedicines. In both studies, the application of electric field–based delivery enhanced particle-tissue interactions but also altered nanoparticle characteristics. Specifically, we observed a significant increase in nanoparticle diameter from 108 nm to 125 nm post-EMDA, accompanied by a reduction in zeta potential from + 18 mV to near-neutral values. Braet et al. similarly reported increased particle size following ePIPAC aerosolization, although the surface charge remained largely stable. This discrepancy may stem from differing mechanisms: EMDA applies directional electroosmosis and ion migration, while ePIPAC relies on electrostatic aerosol dispersion and high shear stress. Despite these mechanistic differences, both studies report maintained colloidal stability, with polydispersity indices (PDI) remaining within the commonly accepted monodisperse threshold (0.226–0.273 in our study). Collectively, these findings support the physicochemical resilience of ionic nanocarriers under external energy fields and reinforce the potential of electro-assisted strategies, whether through direct current (EMDA) or aerosolized electrostatics (ePIPAC), to enhance intraperitoneal nanoparticle delivery in the context of peritoneal metastases.

In tumor-bearing animals, EMDA also improved intratumoral delivery of Cy5-siRNA-RNAiMAX nanoparticles (Figs. 16–18). Enhanced penetration was observed in both macroscopic (>1 cm) and micronodular (<1 cm) tumor nodules, with smaller lesions showing more uniform distribution, likely due to reduced interstitial resistance and less complex stromal architecture. In contrast, larger tumors, despite increased vascularization, demonstrated predominantly peripheral accumulation with limited penetration depth, likely due to elevated interstitial resistance and denser extracellular matrices. These findings are consistent with prior studies reporting that although highly vascularized tumors may accumulate more NPs at the surface, elevated interstitial pressures and stromal density restrict deeper transport [50–53]. Similarly, earlier reports have that smaller tumor volumes allow better NPs uptake under physical enhancement modalities such as iontophoresis or electroporation [4,26,53,54]. Notably, EMDA-treated tumors showed significantly higher MFIs across all ROIs, even in dense lesions, highlighting its capacity to bypass stromal and architectural barriers that limit passive transport.

This outcome aligns with previous EMDA studies. For example, intravesical EMDA has been shown to improve mitomycin C penetration into the bladder wall [16,18,20], and transdermal iontophoresis studies similarly demonstrate current-dependent transport enhancement [10,12,14]. Our results further corroborate computational predictions based on the Nernst–Planck framework, which indicate that transport enhancement is governed by both current magnitude and application time [19,37]. We selected a 1.6 mA current intensity for in vivo application, substantially lower than the 20–30 mA typically used in intravesical protocols, yet sufficient to drive significant particle transport due to the smaller anatomical dimensions in rodents and thus higher local field strength [38]. Importantly, EMDA was well tolerated, with no histological evidence of tissue damage. The observed superiority of EMDA in smaller nodules may be explained by enhanced electric field homogeneity and reduced stromal impedance. These data support findings from Di Stasi et al. and Hashemi et al., which demonstrated EMDA-driven penetration even in fibrotic or poorly vascularized tissues [17,22]. In our study, histological assessments performed at multiple time points during the optimization phase confirmed the absence of tissue damage following short-duration EMDA exposure. However, in a subset of samples exposed for approximately 60 min, mild thickening of the peritoneal membrane was observed, suggesting a localized and potentially transient tissue response. Although these changes were not widespread, they warrant attention when considering longer application times. Future studies should therefore incorporate more detailed, time-resolved histological analyses to further elucidate the cumulative effects of EMDA on host tissue integrity.

Furthermore, our study provides the first in vivo evidence that EMDA enhances nanoparticle delivery specifically in the context of colorectal peritoneal metastases, for which other locoregional therapies such as HIPEC and pressurized IP aerosol chemotherapy (PIPAC) are clinically used [4,44]. Whereas these modalities rely on thermal and pressure gradients, EMDA leverages electrokinetic forces, representing a complementary or alternative strategy, particularly in early-stage disease. These findings complement recent in vivo findings by Min et al [40]. and Van de Sande et al [39], which demonstrated enhanced delivery via electrostatic aerosolization (ePIPAC). However, while those studies focused on charged aerosol deposition, our data highlight the utility of direct current–driven EMDA in liquid-based intraperitoneal delivery, thereby broadening the scope of electro-assisted strategies for IP nanomedicine.

This study establishes proof-of-concept of EMDA-enhanced IP NPs delivery; however, several limitations merit consideration. First, all in vivo investigations were conducted in a single rodent model, employing amine-functionalized fluorescent nanoparticles in healthy peritoneum and siRNA-RNAiMAX complexes in a syngeneic colorectal PM model. Although this dual-system design provided insight into the behavior of distinct nanoparticle classes under EMDA, it introduces formulation-specific variability, potentially confounding direct comparison. Future studies should employ standardized nanoparticle platforms across healthy and malignant conditions to better delineate the contribution of tissue architecture and tumor microenvironment. Second, while we demonstrated significant improvements in IP tissue penetration and regional NPs distribution, the therapeutic implications of this enhanced delivery remain to be established. Future work should include survival analyses and therapeutic efficacy trials to determine whether improved biodistribution translates into clinical benefit.

Third, our study was restricted to a single tumor type colorectal PM. Peritoneal tumors of different origins such as gastric and ovarian cancer differ significantly in their histopathology, stromal composition, and microenvironmental features, all of which can influence electromediated drug and nanoparticle delivery. Gastric PM is typically more fibrotic, poorly vascularized, and diffusely infiltrative, potentially limiting both passive and active transport. In contrast, colorectal PM tends to form discrete nodules with less desmoplasia and better perfusion, while ovarian PM often involves papillary structures and extensive ascitic spread, introducing different barriers to tissue penetration and conductivity. These differences may affect NPs transport, electroporation efficiency, and tissue response to EMDA. As such, further validation in tumor-specific models, including gastric and ovarian PM, is needed to evaluate the broader applicability of this approach. Additionally, the electrokinetic parameters used in this study were optimized for small animal anatomy. The feasibility of EMDA-enhanced IPDD differs from intravesical and dermal applications because of the peritoneum's irregular geometry, variable conductivity, and fluid- and tumor-related heterogeneity, which complicate uniform field generation. Nevertheless, feasibility is supported by sufficient tissue conductivity, our computational and ex vivo human data, and the availability of

laparoscopic or image-guided electrode placement already established in other clinical fields. Translation to humans will require recalibration of current density, electrode configuration, and exposure time, with computational modeling and early-phase clinical trials essential to establish safe and effective conditions.

In conclusion, this study provides the first in vivo evidence that EMDA significantly enhances nanoparticle transport across the peritoneal barrier, including tumor nodules of varying size and density. The approach is well tolerated, scalable, and mechanistically compatible with multiple nanocarrier platforms. These findings establish a strong preclinical foundation for the continued development of EMDA as a novel, electrokinetically driven strategy to improve the locoregional delivery of therapeutics in patients with peritoneal metastases. Future investigations should expand into efficacy testing, survival benefit, repeat dosing feasibility, and validation in diverse tumor types and across species to support eventual clinical application.

Funding

Wim Ceelen is a senior clinical investigator from the Fund for Scientific Research – Flanders (FWO). Annelies Coene is supported by the Fund for Scientific Research – Flanders (FWO) with a senior postdoctoral research fellowship (12Z4722N).

CRediT authorship contribution statement

Mieke Adriaens: Methodology, Investigation, Formal analysis. **Charlotte Debbaut:** Validation, Supervision, Methodology. **Wim Ceelen:** Supervision, Funding acquisition, Formal analysis, Conceptualization. **Annelies Coene:** Supervision, Methodology, Investigation, Formal analysis. **Nidda Saeed:** Writing – review & editing, Writing – original draft, Methodology, Formal analysis. **Jolene Wong Si Min:** Writing – original draft, Methodology, Formal analysis. **Hooman Salavati:** Validation, Methodology, Formal analysis. **Katrien Remaut:** Supervision, Methodology, Investigation. **Sarah Cosyns:** Supervision, Resources, Project administration, Methodology.

Declaration of Competing Interest

None of the author have a conflict of interest to declare.

Data availability

Data will be made available on request.

References

[1] J. Demuytere, S. Ernst, W. Ceelen, Pathophysiology of peritoneal metastasis, J. Surg. Oncol. (2024), 10.1002/jso.27890.
[2] W. Ceelen, et al., Intraperitoneal chemotherapy for peritoneal metastases: an expert opinion, Expert Opin. Drug Deliv. 17 (4) (2020) 511–52210, 1080/17425247.2020.1736551.
[3] W.P. Ceelen, M.F. Flessner, Intraperitoneal therapy for peritoneal tumors: biophysics and clinical evidence, Nat. Rev. Clin. Oncol. 7 (2) (2010) 108–1510, 1038/nrclinonc.2009.217.
[4] N. Lagast, C. Carlier, W.P. Ceelen, Pharmacokinetics and tissue transport of intraperitoneal chemotherapy, Surg. Oncol. Clin. N. Am. 27 (3) (2018) 477–49410, 1016/j.soc.2018.02.003.
[5] H. Salavati, et al., Image-guided patient-specific prediction of interstitial fluid flow and drug transport in solid tumors, J. Control Release 378 (2025) 899–91110, 1016/j.jconrel.2024.12.048.
[6] H. Salavati, et al., Drug transport modeling in solid tumors: a computational exploration of spatial heterogeneity of biophysical properties, Comput. Biol. Med. 163 (2023) 107190, p. 10719010.1016/j.compbiomed.2023.
[7] O. Facy, et al., High pressure enhances the effect of hyperthermia in intraperitoneal chemotherapy with oxaliplatin: an experimental study, Ann. Surg. 256 (6) (2012) 1084–1810, 1097/SLA.0b013e3182582b38.
[8] Y. Bi, et al., Mechanical models and measurement methods of solid stress in tumors, Appl. Microbiol Biotechnol. 108 (1) (2024) 363, https://doi.org/10.1007/s00253-024-13211-, 5.
[9] S. Pan, et al., The journey of nanoparticles in the abdominal cavity: exploring their in vivo fate and impact factors, J. Control Release 376 (2024) 266–28510, 1016/j.jconrel.2024.10.011.
[10] A.K. Banga, Y.W. Chien, Iontophoretic delivery of drugs - fundamentals, developments and biomedical applications, J. Control. Release 7 (1) (1988) 1–24, https://doi.org/10.1016/0168-3659(88)90075-2.
[11] J.B. Phipps, R.V. Padmanabhan, G.A. Lattin, Iontophoretic delivery of model inorganic and drug ions, J. Pharm. Sci. 78 (5) (1989) 365–910, 1002/jps.2600780505.
[12] R.H. Guy, et al., Iontophoresis: electrorepulsion and electroosmosis, J. Control Release 64 (1-3) (2000) 129–3210, 1016/s0168-3659(99)00132-7.
[13] L.P. Gangarosa, et al., Increased penetration of nonelectrolytes into mouse skin during iontophoretic water transport (iontohydrokinesis), J. Pharm. Exp. Ther. 212 (3) (1980) 377–381.
[14] N.A. Charoo, et al., Electroporation: an avenue for transdermal drug delivery, Curr. Drug Deliv. 7 (2) (2010) 125–3610, 2174/156720110791011765.
[15] L. Hughes, D.M. Maurice, A fresh look at iontophoresis, Arch. Ophthalmol. 102 (12) (1984) 1825–1910, 1001/archopht.1984.01040031483028.
[16] W.B. Shelley, P.N. Horvath, et al., Experimental miliaria in man; production of sweat retention anidrosis and vesicles by means of iontophoresis, J. Invest Dermatol. 11 (4) (1948) 275–291.
[17] S. Hashemi, A. Sahai, S. Malde, Applications of electromotive drug administration in urology, Urol. Ann. 12 (4) (2020) 301–30810, 4103/UA.UA_152_19.
[18] S.M. Di Stasi, et al., Electromotive versus passive diffusion of mitomycin c into human bladder wall: concentration-depth profiles studies, Cancer Res 59 (19) (1999) 4912–4918.
[19] T. Gurpinar, et al., Electromotive drug administration to the urinary bladder: an animal model and preliminary results, J. Urol. 156 (4) (1996) 1496–1501.
[20] S.M. Di Stasi, et al., Intravesical electromotive mitomycin c versus passive transport mitomycin c for high risk superficial bladder cancer: a prospective randomized study, J. Urol. 170 (3) (2003) 777–8210, 1097/01.ju.0000080568.91703.18.
[21] S.M. Di Stasi, et al., Sequential BCG and electromotive mitomycin versus BCG alone for high-risk superficial bladder cancer: a randomised controlled trial, Lancet Oncol. 7 (1) (2006) 43–51, https://doi.org/10.1016/S1470-2045(05)70472-1.
[22] S.M. Di Stasi, et al., Electromotive instillation of mitomycin immediately before transurethral resection for patients with primary urothelial non-muscle invasive bladder cancer: a randomised controlled trial, Lancet Oncol. 12 (9) (2011) 871–879, https://doi.org/10.1016/S1470-2045(11)70190-5.
[23] A.Z. Wang, R. Langer, O.C. Farokhzad, Nanoparticle delivery of cancer drugs, Annu Rev. Med 63 (1) (2012) 185–9810, 1146/annurev-med-040210-162544.
[24] K.A. Whitehead, R. Langer, D.G. Anderson, Knocking down barriers: advances in siRNA delivery, Nat. Rev. Drug Discov. 8 (2) (2009) 129–3810, 1038/nrd2742.
[25] N.A.A. Qasem, et al., A comprehensive review of saline water correlations and data: part II-Thermophysical properties, Arab. J. Sci. Eng. 46 (3) (2021) 1941–1979, https://doi.org/10.1007/s13369-020-05020-5.
[26] H. Salavati, et al., Interstitial fluid pressure and hydraulic conductivity in solid tumors: introducing an in-vitro method for measuring the hydraulic conductivity of tumor tissue, Eur. J. Surg. Oncol. 48 (2) (2022) e145–e146.
[27] B. Kos, et al., Investigation of the mechanisms of action behind electromotive drug administration (EMDA), PeerJ 4 (2016) p. e230910.7717/peerj.2309.
[28] G. Giovannetti, et al., An efficient method for electrical conductivity measurement in the RF range, Concepts Magn. Reson. Part B-Magn. Reson. Eng. 37b (3) (2010) 160–166, 10.1002/cmr.b.20165.
[29] I. VilasBoas-Ribeiro, et al., Impact of number of segmented tissues on Sar prediction accuracy in deep pelvic hyperthermia treatment planning, Cancers (Basel) 12 (9) (2020), p. 264610.3390/cancers12092646.
[30] N. Gavish, K. Promislow, Dependence of the dielectric constant of electrolyte solutions on ionic concentration: a microfield approach, Phys. Rev. E 94 (1-1) (2016), p. 01261110.1103/PhysRevE.94.012611.
[31] A.M. Lopes Cardozo, et al., Metastatic pattern of CC531 colon carcinoma cells in the abdominal cavity: an experimental model of peritoneal carcinomatosis in rats, Eur. J. Surg. Oncol. 27 (4) (2001) 359–6310, 1053/ejso.2001.1117.
[32] H. Salavati, et al., Interstitial fluid pressure as an emerging biomarker in solid tumors, Biochim. Biophy. Acta (BBA)-Rev. Cancer (2022) 188792.
[33] K.N. Sugahara, et al., A tumor-penetrating peptide enhances circulation-independent targeting of peritoneal carcinomatosis, J. Control Release 212 (2015), 59–6910.1016/j.jconrel.2015.06.009.
[34] J. Wang, et al., Improving delivery and efficacy of nanomedicines in solid tumors: role of tumor priming, Nanomedicine (Lond) 6 (9) (2011) 1605–2010, 2217/nnm.11.141.
[35] C. Carlier, et al., Tumour tissue transport after intraperitoneal anticancer drug delivery, Int. J. Hyperth. 33 (5) (2017) 534–54210, 1080/02656736.2017.1312563.
[36] D. Hargrove, et al., Tumor specific delivery and radiation-enhanced tumor penetration of mesoporous silica nanoparticles for effective radionuclide therapy of ovarian peritoneal metastasis, Int. J. Pharm. 669 (2025), p. 12507110.1016/j.ijpharm.2024.125071.
[37] D.R. Loke, et al., Simulating drug penetration during hyperthermic intraperitoneal chemotherapy, Drug Deliv. 28 (1) (2021), 145–16110.1080/10717544.2020.1862364.
[38] A.R. Denet, R. Vanbever, V. Preat, Skin electroporation for transdermal and topical delivery, Adv. Drug Deliv. Rev. 56 (5) (2004) 659–7410, 1016/j.addr.2003.10.027.
[39] L. Van de Sande, et al., Electrostatic intraperitoneal aerosol delivery of nanoparticles: proof of concept and preclinical validation, Adv. Health Mater. 9 (16) (2020) p. e200065510.1002/adhm.202000655.

[40] J.W.S. Min, et al., Electromotive enhanced drug administration in oncology: principles, evidence, current and emerging applications, Cancers (Basel) 14 (20) (2022), p. 498010.3390/cancers14204980.
[41] J.H. Jung, et al., Intravesical electromotive drug administration for non-muscle invasive bladder cancer, Cochrane Database Syst. Rev. 9 (9) (2017). CD01186410.1002/14651858.CD011864.pub2.
[42] J. Stachowska-Pietka, et al., Distributed model of peritoneal fluid absorption, Am. J. Physiol. Heart Circ. Physiol. 291 (4) (2006) H1862–H7410, 1152/ajpheart.01320.2005.
[43] H. Salavati, et al., Hydraulic conductivity of human cancer tissue: a hybrid study, Bioeng. Transl. Med 9 (2) (2024) p. e1061710.1002/btm2.10617.
[44] C.M. Agrawal, et al., Effects of fluid flow on the in vitro degradation kinetics of biodegradable scaffolds for tissue engineering, Biomaterials 21 (23) (2000) 2443–2452, https://doi.org/10.1016/s0142-9612(00)00112-5.
[45] L.D. Wright, T. Andric, J.W. Freeman, Utilizing NaCl to increase the porosity of electrospun materials, Mater. Sci. Eng. C. Mater. Biol. Appl. 31 (1) (2011) 30–3610, 1016/j.msec.2010.02.001.
[46] M. Shariati, et al., Aerosolization of nanotherapeutics as a newly emerging treatment regimen for peritoneal carcinomatosis, Cancers (Basel) 11 (7) (2019), p. 90610.3390/cancers11070906.
[47] W. Ceelen, J. Demuytere, I. de Hingh, Hyperthermic intraperitoneal chemotherapy: a critical review, Cancers 13 (13) (2021), p. 311410.3390/cancers13133114.
[48] F. Lugnani, et al., Iontophoresis of drugs in the bladder wall: equipment and preliminary studies, Artif. Organs 17 (1) (1993) 8–1710, 1111/j.1525-1594.1993.tb00378.x.
[49] H. Braet, et al., The effect of electrostatic high pressure nebulization on the stability, activity and ex vivo distribution of ionic self-assembled nanomedicines, Acta Biomater. 170 (2023) 318–32910, 1016/j.actbio.2023.08.027.
[50] R.K. Jain, Transport of molecules across tumor vasculature, Cancer Metastas.. Rev. 6 (4) (1987) 559–9310, 1007/BF00047468.
[51] A. Pluen, et al., Role of tumor-host interactions in interstitial diffusion of macromolecules: cranial vs. Subcutaneous tumors, Proc. Natl. Acad. Sci. USA 98 (8) (2001), 4628–3310.1073/pnas.081626898.
[52] T. Stylianopoulos, R.K. Jain, Combining two strategies to improve perfusion and drug delivery in solid tumors, Proc. Natl. Acad. Sci. USA 110 (46) (2013) 18632–18710, 1073/pnas.1318415110.
[53] E. Ruoslahti, S.N. Bhatia, M.J. Sailor, Targeting of drugs and nanoparticles to tumors, J. Cell Biol. 188 (6) (2010) 759–6810, 1083/jcb.200910104.
[54] M.W. Dewhirst, T.W. Secomb, Transport of drugs from blood vessels to tumour tissue, Nat. Rev. Cancer 17 (12) (2017) 738–75010, 1038/nrc.2017.93.